Applied Catalysis B: Environmental 140–141 (2013) 289–298

Contents lists available at SciVerse ScienceDirect

Applied Catalysis B: Environmental

journal homepage: www.elsevier.com/locate/apcatb

Low-temperature catalytic reduction of NO by NH_3 over vanadia-based nanoparticles prepared by flame-assisted spray pyrolysis: Influence of various supports

Thirupathi Boningari, Rajesh Koirala, Panagiotis G. Smirniotis*

Chemical Engineering Program, School of Energy, Environmental, Biological and Medicinal Engineering, University of Cincinnati, Cincinnati, OH 45221-0012, USA

ARTICLE INFO

Article history:
Received 19 February 2013
Received in revised form 11 April 2013
Accepted 12 April 2013
Available online 22 April 2013

Keywords:
Low-temperature NH_3-SCR
Vanadia (VO_x)
Nitric oxide (NO)
Flame spray pyrolysis

ABSTRACT

A series of V/CeO_2, V/TiO_2, V/Al_2O_3, V/ZrO_2, $V/CeO_2–ZrO_2$, $V/TiO_2–Al_2O_3$, and $V/CeO_2–Al_2O_3$ metal oxide nanoparticles were synthesized by a one-step rapid FSP (flame spray pyrolysis) synthesis technique. Benefiting from the short residence time and high quenching rate during the single-step flame spray process, V^{4+}, V^{3+} ions are successfully incorporated into the crystal lattice of various metal oxide supports. Our XRD, BET studies reveal that the V doping into Al_2O_3, $Al_2O_3–TiO_2$, and $CeO_2–Al_2O_3$ favors the formation of highly dispersed surface vanadia nanoparticles (5.8–9.4 nm), whereas, the V doping into ZrO_2, $CeO_2–ZrO_2$ and CeO_2 led to the primary particle size (19–45.5 nm, formation of bulk particles) growth and thus inhibition in the catalytic activity. It is remarkable to note that the average particle size (nm) of vanadia in our flame-made catalysts has direct relation with the SCR activity. As can be envisaged from XPS spectra, as-synthesized V/ZrO_2 sample primarily consists of V^{5+} species due to the formation of ZrV_2O_7 solid solution as a result of zirconia migration into the V_2O_5 crystallites. Our XPS results imply that the formation of surface V_2O_3 species is improved enormously by the addition of Al_2O_3 ($V^{3+}/V^{n+} = 0.36$, 0.38, and 0.41 for $V/TiO_2–Al_2O_3$, V/Al_2O_3, $V/CeO_2–Al_2O_3$, respectively), whereas, the addition of TiO_2 led to the formation of surface VO_2 species ($V^{4+}/V^{5+} = 0.88$, 1.57 for V/TiO_2, $V/TiO_2–AlO_3$, respectively). Among all the catalysts, high surface $(V^{3+} + V^{4+})/V^{n+}$, and V^{4+}/V^{n+} concentrations were observed for the $V/TiO_2–Al_2O_3$, V/Al_2O_3, $V/CeO_2–Al_2O_3$, respectively. It is highly remarkable to note that the SCR performance of all the as-prepared catalysts is indeed correlated with the surface $(V^{3+} + V^{4+})/V^{n+}$, and V^{4+}/V^{5+} concentrations. The reduction (H_2-TPR) profiles reveal that the vanadium oxide reduction peak has shifted to much lower temperatures in Al-modified catalysts, indicating high reduction potential of the high-coverage VO_x species. This is primarily due to the penetration of the active component into the pores of the support during the flame spray pyrolysis step itself, which in turn, results in a high dispersion of the active component on the support. Clearly, the close proximity of the support to these sites will mean that the support exerts some influence on the behavior of the oxygen species attached to the vanadium. The catalytic performance of various V/M′ (M′ = Ce, Al, Ti, Zr, Ce–Zr, Ti–Al, and Ce–Al) flame-made catalysts (with consistent V content V/M′ = 0.17) was studied for the low-temperature SCR reaction at a range of temperatures (140–360 °C) at gas hourly space velocity (GHSV) = 24,000 h^{-1}. The intrinsic activity of V/Ti–Al, V/Al, V/Ce–Al catalysts with V/M′ = 0.17 atomic ratio measured under differential reaction conditions, was found to be highly active, selective toward nitrogen and broadening the temperature window for optimal operation of this reaction.

Published by Elsevier B.V.

1. Introduction

Vanadium oxides employing titania as the main oxide have been extensively used as supports for the selective catalytic reduction (SCR) of NO_x [1]. The doping of other metal oxides (CeO_2, ZrO_2, Al_2O_3) or mixed metal oxides ($CeO_2–Al_2O_3$, $CeO_2–ZrO_2$, $TiO_2–Al_2O_3$) as support aims at improving the mechanical properties and catalytic performance of the catalysts. WO_3 is used to improve thermal stability, retard the transformation of the anatase phase of titania to rutile [2], and boost the acidity of the support. Our previous studies [3] suggested that the addition of tungsten to V/ZrO_2 promoted the catalyst for the enhancement in the NO conversion, whereas the addition of Mo inhibited the SCR activity. Vanadia catalyst preferably catalyzes the selective transformation

* Corresponding author. Tel.: +1 513 556 1474; fax: +1 513 556 3473.
E-mail address: panagiotis.smirniotis@uc.edu (P.G. Smirniotis).

0926-3373/$ – see front matter. Published by Elsevier B.V.
http://dx.doi.org/10.1016/j.apcatb.2013.04.033

of NO_x to N_2 via a redox cycle [4,5]. Hence, it was established in the literature that the existence of multi oxidation states of vanadium species are required [6–9] for improved catalytic performance and was attributed to the rapid redox cycle of vanadia.

Most research findings suggest the dual-site Eley–Rideal mechanism involving a surface vanadia redox site and an adjacent non-reducible acid–base site [4,5,10,11]. The key and rate-determining step in this mechanism is assumed to be the activated adsorption of ammonia on the V^{5+}—OH Brönsted acid site, which reduces a nearby V^{5+}=O redox site to V^{4+}. This activated intermediate V^{4+}—OH, is very reactive toward gaseous NO, leading to the products, N_2 and H_2O, which desorb from the surface [8–13]. Other researchers also reported that the use of low valance vanadia (V^{4+}, V^{3+}) catalysts enhance the NO conversions and selectivity up to 60% [6–9].

On the other hand, vanadium oxide catalysts supported on various metal oxides such as Al_2O_3, TiO_2, CeO_2 and ZrO_2 are industrially important active catalysts [14–17]. Catalysts made up of vanadia supported on or mixed with other metal oxides have been studied quite extensively [1,18] because of their use in several industrial heterogeneous catalytic processes. Such as the oxidative destruction of volatile organic compounds [19,20], ammoxidation of oxidation of hydrocarbons (butene, benzene, *o*-xylene, and naphthalene) to anhydrides [19,20], oxidation of SO_2 to SO_3 [21–23], and selective catalytic reduction (SCR) of nitrogen oxides [3,24–26]. However, the state of the supported oxides and their transformations under catalytic reduction reaction conditions are not fully understood.

Herein, the catalytic performance of various V/M′ (M′ = Ce, Al, Ti, Zr, Ce–Zr, Ti–Al, and Ce–Al) flame-made catalysts (with consistent V content V/M′ = 0.17) was studied for the low-temperature SCR reaction at a range of temperatures (140–360 °C) at gas hourly space velocity (GHSV) = 24,000 h^{-1}. The intrinsic activity of V/Ti–Al, V/Al, V/Ce–Al catalysts with V/M′ = 0.17 atomic ratio measured under differential reaction conditions, was found to be highly active, selective toward nitrogen and broadening the temperature window for optimal operation of this reaction. The V 2*p* peaks demonstrate broadening of the line with alumina, titania, and ceria doping compared to the zirconia doping. This broadening of XPS peaks attributed to the presence of more than one type of V^{5+} or V^{4+} species, and the electron transfer between the active component and the support. Our TPR results also suggest that the vanadium might have stabilized as the reduced vanadia oxidation states on the Al_2O_3 support up to monolayer coverage, probably due to removal of a bridge oxygen from a V—O—V linkage in surface vanadia species. This contribution presents the use of spectroscopic, physico-chemical techniques to study the effect of various supports in the molecular structure, crystallite size, reduction profiles and oxidation state of surface vanadium oxide cations for the selective catalytic reduction at low-temperatures. The relative extents of the surface atomic concentrations of V^{5+}, V^{4+}, and V^{3+}, particle size measurements, reduction of vanadia species, were examined using XPS, BET, H_2-TPR analysis, respectively.

2. Experimental

2.1. Catalysts preparation

A series of V_2O_5/CeO_2, V_2O_5/TiO_2, V_2O_5/Al_2O_3, V_2O_5/ZrO_2, $V_2O_5/CeO_2–ZrO_2$, $V_2O_5/TiO_2–Al_2O_3$, and $V_2O_5/CeO_2–Al_2O_3$ metal oxide nanoparticles were synthesized by a one-step rapid FSP synthesis technique. The spray apparatus consists of a syringe infusion pump (Cole-Parmer, 74900 series), MKS mass flow controllers, and an FSP reactor, which is made from two concentric tubes and a coil tube with seven evenly distributed pores (0.37 mm) surrounding the two inner tubes [27]. One inner tube has an inner diameter of 1.02 mm, and the other one has an inner diameter of 0.51 mm (outer diameter of 0.82 mm). Vanadyl (V) tri-i-propoxy oxide (Strem Chemicals) was dissolved in *Ortho*-xylene (Sigma–Aldrich Reagent, 98%) with the corresponding metal precursors for the respective metal oxide support (cerium (III) 2-ethylhexanoate 49% in 2-ethylhexanoic acid, Strem Chemicals (12.20% Ce), titanium (IV) 2-ethylhexoxide, Strem Chemicals, (84% Ti), aluminum acetylacetonate (Aldrich, 99.99%), and zirconyl 2-ethylhexanoate, Strem Chemicals, ~6% Zr). The total molar concentration of V + X (X = Ce, Ti, Al, Zr, Ce + Zr, Ti + Al, and Ce + Al) in the liquid precursor was set at the range from 0.1 to 0.5 M. Throughout the synthesis of catalysts by FSP, the liquid precursor was fed through a spray nozzle at a flow rate of 2 mL min^{-1} using a syringe pump, where it was dispersed by a surrounding 5 L min^{-1} flow of oxygen (1.5 bar, Wright Brothers, 99.98%). Combustion of the dispersed droplets was ignited by a surrounding supporting flame (premixed 1.0 L min^{-1} O_2/0.85 L min^{-1} CH_4). Fine aerosol nanoparticles leaving the flame were collected on a flat glass fiber filter (Whatman GF/A, 150 mm in diameter) aided by a vacuum pump (Grainger Inc.). The aerosol nanoparticles were scraped from the filter for direct use as catalyst without any further treatment. The metal components of the catalysts are denoted as atomic ratios. The various supports were used to ensure the promoting effect on NO conversions in the SCR reaction. All the ratios of the catalysts in this study are V/M′ = 0.17.

2.2. X-ray diffraction

Phillips X'pert diffractometer was used to collect diffraction patterns of all the FSP-made catalysts (V_2O_5/CeO_2, V_2O_5/TiO_2, V_2O_5/Al_2O_3, V_2O_5/ZrO_2, $V_2O_5/CeO_2–ZrO_2$, $V_2O_5/TiO_2–Al_2O_3$, and $V_2O_5/CeO_2–Al_2O_3$) using a nickel filtered Cu-Kα radiation (wavelength 0.154056 nm) source and a scintillation counter detector. The as synthesized catalysts were placed on an aluminum holder. The intensity data were collected over a 2θ range of 20°–80° with a step size of 0.025° and with a scanning rate of 1 s/point. All the crystalline phases were identified by comparison with the reference data from International Center for Diffraction Data (ICDD) files.

2.3. BET surface area and pore volume measurements

The BET specific surface area of the as-prepared nanoparticles was determined from nitrogen adsorption equilibrium isotherms at liquid nitrogen temperature (77 K) using an automated gas sorption system (Micromeretics ASAP 2010) operating in continuous mode. Prior to the analysis, 0.015–0.020 g of catalysts were evacuated under helium atmosphere for 2 h at 200 °C in the degassing port of the instrument. Specific surface area (SSA) was calculated at 77 K using a six-point N_2 adsorption isotherm recorded in a relative partial pressure (p/p_0) range of 0.05–0.99, and by taking 0.162 nm^2 as the molecular area of the nitrogen molecule. Pore volume was calculated at the relative pressure of about 0.99 using a single-point adsorption value.

2.4. Transmission electron microscopy (TEM)

As-synthesized V/Al_2O_3 samples were characterized with a Philips CM 20 electron microscope. The samples were sonically dispersed in *iso*-propyl alcohol and transferred onto a carbon copper grid. After complete evaporation of the alcohol, the particles attached on the walls of holes in the carbon film were examined. The applied accelerating voltage was 200 keV, with a LaB6 emission current and a point-to-point resolution of 0.27 nm.

2.5. Temperature programmed reduction (H_2-TPR)

The hydrogen-temperature programmed reduction experiments of as-prepared aerosol nanoparticles were performed using an automated catalyst characterization system (Micromeritics model AutoChem 2910). Prior to the analysis approximately 0.030 g of catalysts were pre-treated at 200 °C for 2 h in ultra high pure helium (30 mL min^{-1}) stream. Subsequently, samples were tested by increasing the temperature from 50 to 800 °C. The temperature was then kept constant at 800 °C until the signal of hydrogen consumption returned to the initial values. The temperature programmed reduction runs were carried out with a linear heating rate of 10 °C min^{-1} in a flow of 10% H_2 in argon with a flow rate of 20 mL min^{-1}. The hydrogen consumption was measured quantitatively by a thermal conductivity detector. A mixture of isopropanol and liquid nitrogen was used in the trapper to collect the formed water during the TPR experiment.

2.6. X-ray photoelectron spectroscopy (XPS)

XPS was used to analyze the atomic surface concentration on each catalyst. The X-ray photoelectron spectroscopy (XPS) experiments were carried out on a Pyris-VG thermo scientific X-ray photoelectron spectrometer system equipped with a monochromatic AlK_α (1486.7 eV) as a radiation source at 300 W under UHV (6.7×10^{-8} Pa). Sample charging during the measurement was compensated by an electron flood gun. The electron takeoff angle was 45° with respect to the sample surface. The spectra were recorded in the fixed analyzer transmission mode with pass energies of 89.45 and 35.75 eV for recording survey and high resolution spectra, respectively. The powdered catalysts were mounted onto the sample holder and evacuated overnight at room temperature at a pressure on the order of 10^{-7} torr. Binding energies (BE) were measured for C 1*s*, O 1*s*, V 2*p*, Ti 2*p*, Al 2*p*, Ce 3*d*, and and Zr 3*d*. Sample charging effects were eliminated by correcting the observed spectra with the C 1*s* binding energy (BE) value of 284.6 eV. An estimated error of ±0.2 eV can be considered for all the measurements. The overlapped V 2*p* peaks were deconvoluted into several sub-bands by searching for the optimal combination of Gaussian bands with the correlation coefficients (r^2) above 0.99. The V 2*p* peak was deconvoluted using the Gaussian function.

2.7. Apparatus and catalytic experiments

The potential catalytic performance of the prepared aerosol nanoparticles in the low-temperature SCR of NO by NH_3 with excess oxygen was tested at atmospheric pressure in a continuous flow fixed bed quartz reactor. The predetermined amount of as-synthesized catalyst was placed in the reactor in between two glass wool plugs. All the gas flows were measured and calibrated using a digital flow meter (Humonics Hewlett Packard Optiflow 520). The typical reactant gas composition was as follows: 400 ppm NO, 400 ppm NH_3, 2 vol% O_2 and ultra high purified helium (UHP helium 99.999%) as balance. The premixed gases oxygen (4% in He, Wright Brothers), ammonia (3.99% in He, Wright Brothers) and nitric oxide (2.0% in He, Matheson) were used as received. The reactor was heated externally via a tubular furnace regulated by a temperature controller (Omega CN 2041), with a thermocouple inserted into the catalyst bed. The NO and NO_2 concentrations were continually monitored by a chemiluminescence NO/NO_x detector (Eco Physics CLD 70S). Prior to the catalytic experiments, the catalyst was activated *in situ* by passing 2 vol.% oxygen (4% in He, Wright Brothers) for 2 h at 200 °C temperature. The reactants and products were analyzed *on-line* using a Quadrapole mass spectrometer (MKS PPT-RGA), and a chemiluminescence NO/NO_x detector (Eco Physics CLD 70S). Reactant and product contents in the reactor effluent were recorded at 6 h of continuous reaction at each temperature step.

3. Results and discussion

3.1. Crystallite and surface characterization of V/M′ (M′ = Ce, Ti, Al, Zr, Ce–Zr, Ti–Al, and Ce–Al) catalysts

The specific surface area (S_{BET} m^2/g), porevolume measurements of vanadia based flame made catalysts, obtained by N_2 physisorption at −197 °C, have shown in Table 1. Among all the catalysts prepared, 15V–Al_2O_3, 15V–TiO_2–Al_2O_3 catalysts showed high surface area (168.2 m^2/g, 125.8 m^2/g), and high porevolume (0.43 cm^3/g, 0.36 cm^3/g), respectively. This is primarily due to the penetration of the active component into the pores of the support during the flame spray pyrolysis step itself, which in turn, results in a high dispersion of the active component on the support. Our previous XRD studies [3] suggested that the vanadia species are in amorphous state two-dimensional structure of VO_x species on zirconia support in V/ZrO_2 samples with V/Zr ≤ 0.17. Further increase in vanadia content led to the formation of ZrV_2O_7 solid solution as a result of zirconia migration into the V_2O_5 crystallites and thus leading to the inhibition in the catalytic activity. The diffractogram patterns of pure V_2O_5 sample, the strong characteristic peaks of vanadia typically at 2θ = 20.1°, 25.4°, 26.6°, 36.1°, 37.3°, 39.4°, 46.3° (JCPDS-ICDD 9-387), and ZrV_2O_7 (2θ = 17.4°, 20.1°, 22.5°, 24.6°,

Table 1
Specific surface area and pore volume measurements of as-synthesized V based flame-made catalysts.

Sample[a]	XRD phases	SSA (m^2/g)	Pore diameter (nm)	Pore volume (cm^3/g)	Average[b] particle size (nm)
ZrO_2	T, M	89	12.0	0.52	–
Al_2O_3	–	200	12.4	0.62	–
CeO_2	–	167	11.1	0.46	–
CeO_2–Al_2O_3	–	136	11.4	0.38	–
TiO_2–Al_2O_3	–	164	10.0	0.41	–
CeO_2–ZrO_2	–	126	17.4	0.53	–
TiO_2	A, R	101	15.0	0.29	–
V_2O_5	V_2O_5	14.5	9.95	0.03	–
V–Ce	CeO_2	51.7	8.02	0.10	19.0
V–Ti	A, R	30.1	6.19	0.05	32.6
V–Zr	T, M	22.0	14.4	0.11	44.5
V–Al	α-Al_2O_3, γ-Al_2O_3	168	10.0	0.43	5.8
V–Ce–Zr	CeO_2, T, M	26.2	5.43	0.04	37.5
V–Ce–Al	CeO_2, α-Al_2O_3, γ-Al_2O_3	104	10.1	0.27	9.4
V–Ti–Al	–	126	11.1	0.36	7.8

[a] V/support atomic ratio = 0.17; A, anatase (TiO_2); R, rutile (TiO_2); T, tetragonal (ZrO_2); M, monoclinic (ZrO_2).
[b] Active particle size of vanadia-based nanoparticles determined by BET-specific surface area measurements.

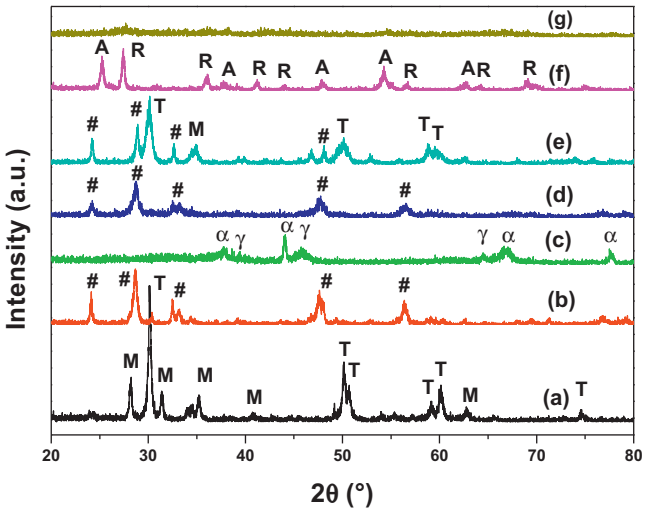

Fig. 1. Powder X-ray diffraction patterns of the FSP-made vanadia-based catalysts (a) 15V/ZrO_2, (b) 15V/CeO_2, (c) 15V/Al_2O_3, (d) 15V/CeO_2–Al_2O_3, (e) 15V/CeO_2–ZrO_2, (f) 15V/TiO_2, and (g) 15V/TiO_2–Al_2O_3; M, monoclinic (ZrO_2); T, tetragonal (ZrO_2); #, cerianite (CeO_2); α, α-phase (Al_2O_3); γ, γ-phase (Al_2O_3); A, anatase (TiO_2); R, rutile (TiO_2).

46.1°, 54.3° (JCPDS 16-422) formed as a result of zirconia migration into the V_2O_5 crystallites when the vanadium loading increases [3,28,29]. These results show that the XRD peaks of individual crystalline V_2O_5 or zirconium pyrovanadate (ZrV_2O_7) are absent up to the 15 wt.% loading level of vanadia. This is a clear indication that the monolayer dispersion of vanadium oxide species attained with 0.17 atomic ratio of V/Zr content. These results are in consistent with the literature, where the monolayer of vanadium oxide species attained with this amount of vanadia [1,30]. For this reason, we have prepared vanadia based catalysts using various supports with V/M′ (M′ = Ce, Ti, Al, Zr, Ce–Zr, Ti–Al, and Ce–Al) = 0.17 atomic ratio.

The X-ray powder diffraction patterns of all the as-prepared FSP-made catalysts (V/CeO_2, V/TiO_2, V/Al_2O_3, V/ZrO_2, V/CeO_2–ZrO_2, V/TiO_2–Al_2O_3, and V/CeO_2–Al_2O_3) have shown in Fig. 1. As can be seen from the figure, the V/ZrO_2 sample shows sharp diffraction peaks at 2θ = 30°, 35°, 51°, 59.4°, 60°, 62.7° and 74.6° (JCPDS 14-534), corresponding to the presence of the tetragonal phase, and diffraction peaks at 2θ = 28°, 31.2°, 35.1°, 40.9° which indicates the presence of the monoclinic phase (JCPDS 36-420) [31]. All the peaks of V/CeO_2 sample in the XRD spectra shows sharp diffraction peaks at 2θ = 24.1°, 28.6°, 32.6°, 48.1°, 56.4°, and 59.2° (JCPDS-34-0394), which are perfectly indexed as the 111, 200, 220, 311, and 222 planes of pure cubic phase (*Fm*.3*m*, JCPDS-34-0394) of CeO_2 nanoparticles [32]. For V/TiO_2 sample, the strong characteristic peaks of titania typically at 2θ = 25.4°, 37.8°, 47.9°, 54.5°, and 62.5°, which corresponds to the (1 0 1), (0 0 4), (2 0 0), (1 0 5 and 2 1 1) planes of the anatase phase (JCPDS #71-1272), as well as 2θ = 27.5°, 36.1°, and 56.6°, which are attributed to (1 1 0), (1 0 1), (2 1 1) planes of the rutile phase (JCPDS# 21-1276) can be observed [33]. X-rays diffraction analysis of V/Al_2O_3 sample indicates that the γ-Al_2O_3 (cubic) and (α-Al_2O_3, trigonal/rhombohedral) corundum phases (JCPDS# 47-1308, JCPDS# 83-2080, respectively) formed during the flame spray pyrolysis process [34]. Our present XRD studies revealed that the promoter oxide does not favor any mixed oxide formation. No vanadium phase could be detected in any sample ≤15 wt.% vanadia, indicating that the VO_x species are in a highly amorphous state and also insertion of vanadium ions into the support lattice. The active metal oxide species itself are in amorphous or highly dispersed state in all the catalysts. The highly dispersed state of vanadia species could extensively increase existence of surface oxygen vacancies and the amount of active sites over the catalyst surface.

The mass fraction of anatase and rutile in the V/TiO_2 sample was determined from the relative XRD diffraction intensities corresponding to the anatase {1 0 1}, rutile {1 1 0} reflections. The mass fraction of anatase and rutile were determined using Eqs. (1) and (2) [35–37].

$$\text{Anatase}\,(\%) = \left[\frac{0.79\,I_A}{0.79I_A + I_R}\right] \times 100 \quad (1)$$

$$\text{Rutile}\,(\%) = \frac{1}{[(I_R + 0.79I_A)/I_R]} \times 100 \quad (2)$$

where I_A, and I_R are the peak intensities of anatase {1 0 1}, rutile {1 1 0} reflections, respectively. λ the wavelength of the X-ray radiation (0.15406 nm) and θ is the diffracting angle.

From the line broadening of corresponding X-ray diffraction peaks, the average crystallite size were determined according to the Scherrer equation (Eq. (3)) by fitting the peaks using a Voigt function

$$D = \frac{0.9\lambda}{\beta\cos\theta} \quad (3)$$

where β is the line width at medium height, λ the wavelength of the X-ray radiation (0.15406 nm) and θ is the diffracting (Bragg) angle. The average particle size was estimated by assuming all the particles to have the same spherical shape and size. The average particle diameter, *d*, is given by Eq. (4):

$$d = \frac{6}{S_{BET} \times \rho_a} \times 1000 \quad (4)$$

where S_{BET} is the specific surface area per unit mass of the sample and ρ_a is the true density. ρ_a for vanadium oxide is 6.11 g/cc. The average particle sizes of as-synthesized vanadia-based materials are induced in Table 1.

The TEM images of selected as-prepared V/Al_2O_3 nanoparticles are presented in Fig. 2. As shown in the figure, a uniform distribution of nanoparticles can be observed. Particle sizes of the V/Al_2O_3 are 4–10 nm. These results are in consistent with our BET analysis (Table 1) where the V/Al_2O_3 sample exhibits the lowest average particle size (5.8 nm) among all the as-synthesized catalysts.

3.2. *Effect of vanadia particle size, porevolume, and textural properties on the SCR activity*

For an adequate determination of effect of the surface textural properties on the NO conversions profile of the V-based flame-made catalysts, we have compared surface porevolume of the catalysts with SCR activity. The corresponding profiles are presented in Fig. 3. The porevolume of our V-based catalyst has direct impact on their SCR activity. In other words, the Al-doping has a strong influence on the NO conversion, since all the Al-doped catalysts with the V/M′ ratio = 0.17 (M′ = Al, Ti–Al, Ce–Al) catalysts exhibit a maximum porevolume and high NO conversion at 320 °C (Fig. 3). On the other hand, the average particle size (nm) of vanadia in all the prepared catalysts has significant effect on the selective reduction reaction of NO (Fig. 4). It is highly remarkable to note that the average particle size (nm) of vanadia in our flame-made catalysts has direct relation with the SCR activity. The NO conversions monotonically increased with decrease in average particle size of vanadium oxide species and the NO conversions drastically declined with increase in particle diameter. Doping of the vanadia-based catalysts with Al_2O_3 led to the formation of surface nanoparticles (5.8–9.4 nm) whereas, the doping with other metals (ZrO_2, CeO_2–ZrO_2, TiO_2, and CeO_2) leading to the formation of bulk

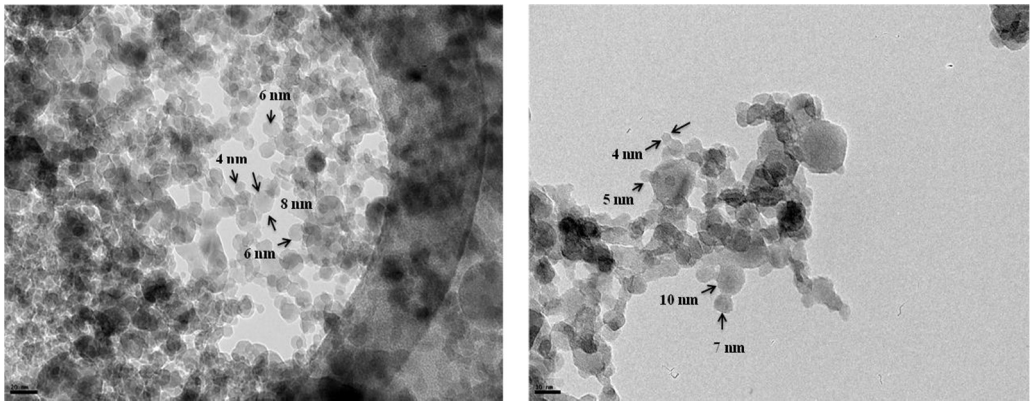

Fig. 2. TEM images of as-synthesized V/Al_2O_3 nanoparticles.

particles (19–45.5 nm). Correspondingly, the resultant highly dispersed and high porevolume of flame-made nanoparticles increase the surface area and thus enhance the catalytic reduction of NO over V/Al_2O_3, V/TiO_2–Al_2O_3, and V/CeO_2–Al_2O_3 catalysts. The other metals such as zirconia, titania, ceria in 0.3 M concentration of the precursor droplets with the provided residence time in the flame-reaction zone leading to higher particle collisions resulting in particle diameter growth, which reduced the surface area of the material especially when coalescence takes place. As expected, there is a little inverse relation between SCR activity and average particle size of vanadia. It is because the isolated surface polymeric vanadium oxide species have been described to destabilize the texture of the support [38,39]. The high porevolume and the surface nanoparticles seem to be the reason for the high activity of flame-made alumina doped vanadia catalysts. Remarkably, the entire Al-doped vanadia-based catalysts exhibit much higher NO conversions and broadening of the temperature window compared to the Zr-, Ti-, Ce-doped sorbents. Both V/Al, and V/Ti–Al (0.17 atomic ratio) exhibit higher activity and better selectivity compared to V/Zr, V/Ce–Zr, V/Ti and V/Ce (0.17) catalysts. On the whole, our results show that the doping of vanadia flame-made catalysts with Al increase the surface concentration of vanadium nanoparticles and thus enhance the SCR activity as well as broadens the temperature window.

A series of V_2O_5/CeO_2, V_2O_5/TiO_2, V_2O_5/Al_2O_3, V_2O_5/ZrO_2, V_2O_5/CeO_2–ZrO_2, V_2O_5/TiO_2–Al_2O_3, and V_2O_5/CeO_2–Al_2O_3 metal oxide nanoparticles were synthesized rapidly in a direct flame spray pyrolysis using 0.3 M precursor solution, showing composition dependent porevolume and specific surface areas of 0.05–0.43 $cm^3\ g^{-1}$, 22.0–168.2 $m^2\ g^{-1}$, respectively (Table 1). In the absence of vanadia content, i.e. pure Al_2O_3, showed high specific surface area. As expected, there is a minimal decrease in SSA and porevolume of the Al-doped samples. It can be seen that the porevolume and specific surface area of other catalysts (Zr-, Ti-, Ce-doped) were drastically dropped to 0.04 $cm^3\ g^{-1}$ and 22 $m^2\ g^{-1}$, respectively. The total molar concentration of the precursor solutions also has significant impact on particle size and morphology [40–42]. As we described earlier [3], vanadia nanoparticles were made by FSP using wide range of molar concentration (0.1–0.5 M) of ZrO_2 precursor solutions. The BET surface area and pore volume of the pure ZrO_2 monotonically increased with increasing the molar concentration and attained maximum value of 89.3 m^2/g and 0.52 cm^3/g, respectively at 0.3 M [3]. Further increase in the total molar concentration of the precursor drastically decreased the specific surface area and pore volume of the nanoparticles. The mass fraction of anatase and rutile in the V/TiO_2 samples was determined from the relative XRD diffraction intensities corresponding to the anatase {1 0 1}, rutile {1 1 0} reflections to ensure the effect of Al-doping into V/TiO_2 sample. The determined mass fraction of anatase and rutile for the V/TiO_2 sample were 39%, and 61%, respectively.

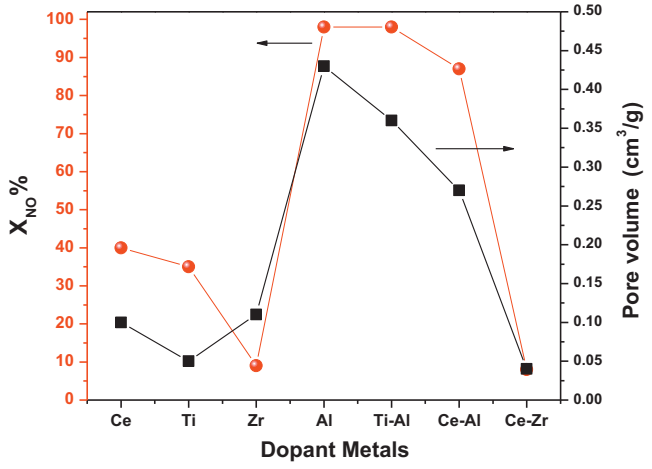

Fig. 3. Correlation between the NO conversions and the porevolume of the V-based FSP catalysts.

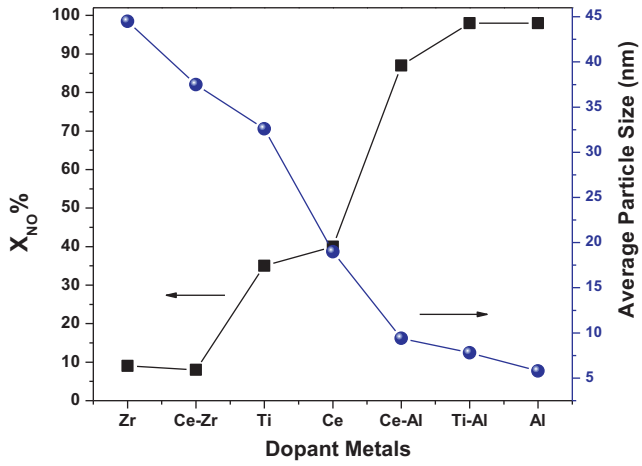

Fig. 4. Relationship between average particle size and NO conversions.

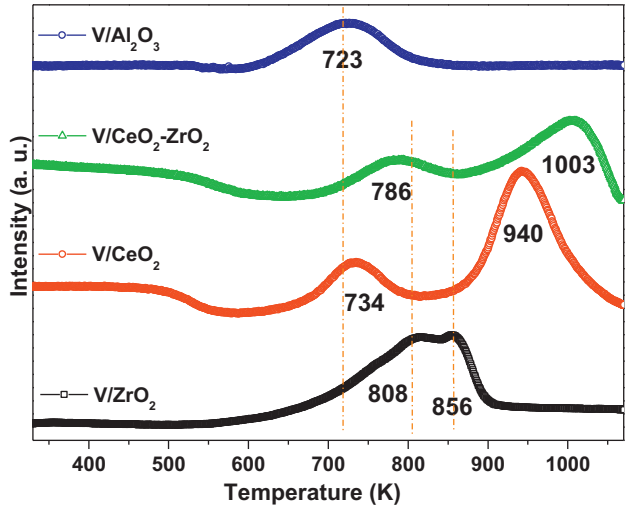

Fig. 5. H_2-temperature programmed reduction patterns of as-synthesized V based flame-made catalysts (a) V/ZrO_2, (b) V/CeO_2, (c) V/CeO_2–ZrO_2, (d) V/Al_2O_3.

3.3. Temperature-programmed reduction (H_2-TPR): support effects on reduction profile of flame-made vanadia nanoparticles

In order to obtain the information about the active metal species for the low-temperature SCR reaction, we have carried out the H_2-temperature programmed reduction of all the as-synthesized catalysts. Temperature-programmed reduction in the presence of H_2 (TPR) provided significant information on the reducibility of the prepared catalysts. Figs. 5 and 6 show the H_2 consumption curves obtained as a function of temperature for the V-based flame-made nanoparticles with 0.17 atomic ratio containing either metal dopant (Ce, Zr, Ti, Al) or mixed oxide dopants. Three distinctive reduction peaks at 863 K (T_1), 927 K (T_2) and 1010 K (T_3) were evident in the TPR profile for the pure vanadia sample [3]. A similar observation has been reported in the literature [38,39,43]. When vanadia was supported on CeO_2, the TPR peaks were broad and less defined than in the case of vanadia supported on Al_2O_3 (Fig. 5). Nevertheless, the peaks having maxima between 610 and 800 K can be assigned to highly dispersed isolated monomeric or dimeric species of vanadia. The V/Ce, V/Ce–Al, V/Ce–Zr catalysts show an additional peak in the range of 900–1050 K which is attributed to the reduction of bulk CeO_2 (Figs. 5 and 6). Regardless of the type of ceria or addition of metal, a peak around 900–1050 K ascribed to the reduction of bulk oxygen of CeO_2, remains unchanged for all the Ce-modified samples. These results are highly consistent to the case of Au–Ce nanoparticles [44] or on ceria–zirconia oxide solid solutions [45]. Other transition metals and metal oxides on ceria have a similar effect [46–48]. It can be noted from all the Ce-doped vanadia catalysts that the bulk CeO_2 reduction peak is highly dominant over the vanadia reduction peak. For this reason, we have excluded the area of the bulk ceria reduction peak for the vanadia nanoparticles dispersion measurements. However, in the case of V/Ce–Al the latter peak (high temperature peak) is much smaller than the one observed for the vanadia reduction, which indicates a better dispersion of vanadia when compared to the other Ce-doped vanadia catalysts. It should be noticed that the Al_2O_3 has a higher specific surface area than the ZrO_2, TiO_2, and CeO_2 which allows a better dispersion of the loaded vanadia. The Al-modified vanadia catalysts shows no bulk vanadia formation (isolated polymeric V oxides species) peak at around 850 K, and no bulk ceria, alumina reduction peak at around 900–1050 K. The disappearance of high temperature peak (900–1050 K) in V/Al, V/Ti–Al suggests that the isolated monomeric vanadium species are highly dominant in Al-modified vanadia nanoparticles.

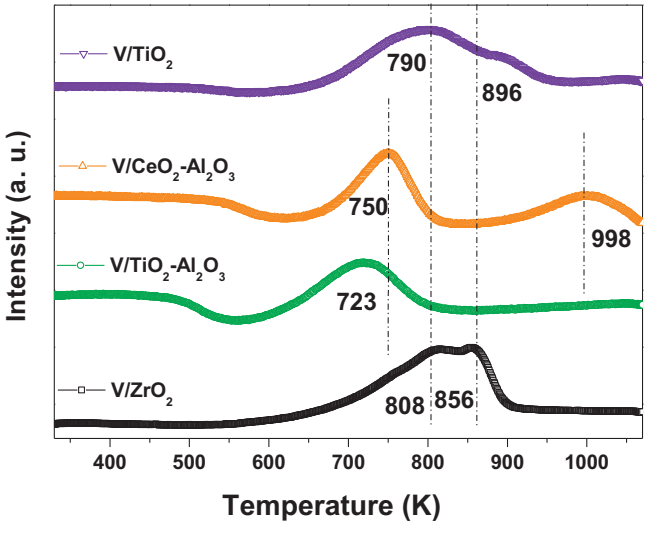

Fig. 6. H_2-temperature programmed reduction patterns of as-synthesized V based flame-made catalysts (a) V/ZrO_2, (b) V/TiO_2–Al_2O_3, (c) V/CeO_2–Al_2O_3, (d) V/TiO_2.

Table 2
Hydrogen uptake, active metal dispersion and temperature reduction steps of all the as-synthesized catalysts.

Catalyst	T (K)[a]		m^2/g[b]	H_2 consumption ($\mu mol\ g^{-1}$)
	T_1	T_2		
$15V/TiO_2$	790	896	107.7	4937
$15V/Al_2O_3$	723	–	127.4	3109
$15V/CeO_2$	734	940	16.1	6209
$15V/ZrO_2$	808	856	51.9	4418
$15V/TiO_2$–Al_2O_3	723	–	63.6	3583
$15V/CeO_2$–ZrO_2	786	1003	16.1	6209
$15V/CeO_2$–Al_2O_3	750	998	58.9	4424

[a] Temperature maxima at low-temperature (T_1); at high-temperature (T_2).
[b] Fraction of vanadia atoms at the surface calculated from chemisorption.

As one can observe from Fig. 5, the two reduction peaks at 808 and 856 K were overlapped in the H_2-TPR profile of V/ZrO_2 catalyst. The low-temperature reduction peak can be assigned to the reduction of surface monomeric VO_x species. A second and stronger peak is observed at temperatures at 856 K peak maxima, which can be attributed to the reduction of bulk vanadium oxide (isolated polymeric vanadium oxide) species. The V/Al, V/Ti–Al catalysts show only one strong peak of H_2 consumption, centered at around 723 K, which denotes the presence of monomeric VO_x species layer over the Al_2O_3 support. The vanadium oxide reduction peak has shifted to much lower temperatures in Al-modified catalysts, indicating high reduction potential of the high-coverage VO_x species. This low temperature shifts in the reduction peaks can be attributed to the presence of more easily reducible highly dispersed dominant surface monomeric VO_x species. The evolution of a new reduction peak at high temperature in Ce-doped vanadia materials indicates the formation of dominantly isolated polymeric V oxides species [49]. We can clearly observe the increase in the reducibility of V species in V/Ce–Al when compared to V/Ce reduction profile. Hence, we consider any significant increase in the reduction potential of vanadium species with Al-doping as suggestive of a structural difference in the surface VO_x species. These results are in consistent with Our XRD (Fig. 1), and average particle size results (Table 1) where the vanadium oxide species are in highly dispersed amorphous state in Al-modified catalysts.

Quantitative hydrogen consumption analysis (Table 2) shows that the reducibility of the vanadia species (H_2 consumption) is high in the case of Al-doped vanadia flame-made catalysts, whereas the

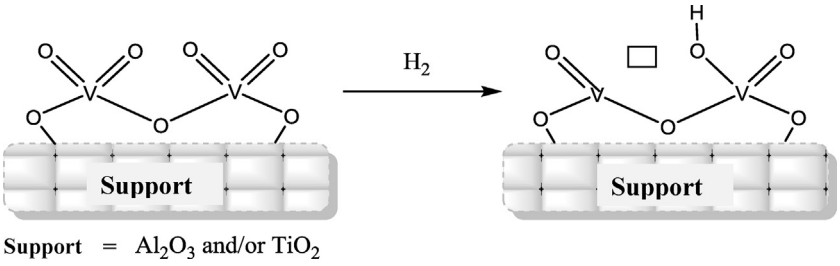

Fig. 7. Anchoring of vanadium oxide species onto a support and the generation of oxygen vacancy.

reducibility of V-species decreased with other metal-dopants (Ce-, Zr-, Ti), due to the decline in surface concentration of vanadium species (Table 2). Enhancement in the reduction potential of vanadia species and highly dispersed state of surface monomeric VO_x species seem to be the reason for high SCR activity, of V/Al, V/Ti–Al catalysts. These results are in high agreement with the SCR activity results, where the addition of Al demonstrated high NO conversion, and broad temperature window whereas the addition of Zr, Ce, Ti showed narrow temperature window for the SCR of NO reaction. The NO conversion decreased drastically at high temperatures in V/Ce–Zr, V/ZrO_2, V/TiO_2, V/CeO_2 catalysts, respectively, which may be caused by the blocking effect of the surface active pores by the particle size growth. Apparently, the alumina support stabilizes vanadia species in the reduced state. However, another justification can be offered, based on a proposed model of Haber et al. [50]. These authors envisage a dimeric V—O structure bonded to the alumina surface for the oxide catalyst, which consumes 1.5 mol of H_2 (instead of 2 mol for the reduction of V_2O_5 to V_2O_3). The V^{3+}, V^{4+} states are apparently stabilized on the $A1_2O_3$, TiO_2 (Fig. 7) but not on other metal oxide surfaces where □ represents an anion vacancy in the surface vanadia structure. According to Topsøe et al. [4], the regeneration of the V^{5+}=O species occurs through two steps, which involve the production of V^{4+} and the oxidation of this reduced species by gaseous O_2. The reaction mechanism [51] is also consistent with the suggestion that partial reduction of the catalyst occurs in the early stages as it also suggests the presence of surface V^{4+} species over the support metal oxide. Clearly, the close proximity of the support to these sites will mean that the support exerts some influence on the behavior of the oxygen species attached to the vanadium.

3.4. X-ray photoelectron spectroscopy

To gain additional insight about the oxidation state of vanadia species and to ensure the chemical compositions (atomic concentrations) of the surface layer, XPS spectra of the samples were recorded. The V 2*p* and O1s XPS spectra of the vanadium oxides V_2O_5, VO_2 and V_2O_3 were measured by Demeter et al. [52] to the vanadium oxidation states V^{5+}, V^{4+} and V^{3+}. However, two main peaks due to V $2p_{3/2}$ and V $2p_{1/2}$ of our vanadia-based materials (V_2O_5/CeO_2, V_2O_5/TiO_2, V_2O_5/Al_2O_3, V_2O_5/ZrO_2, $V_2O_5/CeO_2–ZrO_2$, $V_2O_5/TiO_2–Al_2O_3$, and $V_2O_5/CeO_2–Al_2O_3$) are shown in Fig. 8. It has been well established in the literature that the binding energies of $V^{5+}2p_{3/2}$, $V^{4+}2p_{3/2}$, and $V^{3+}2p_{3/2}$ peaks appear in the range of 517.5 ± 0.2, 516.2 ± 0.2, and 515.8 ± 0.2 eV, respectively [52,53]. Atoms of a higher positive oxidation state exhibit a higher binding energy due to the extra coulombic interaction between the photo-emitted electron and the ion core. This ability to discriminate between different oxidation states and chemical environments is one of the major strengths of the XPS technique. For the identification of the surface vanadium oxide phases and the relative percentages of V^{n+}/M', V^{5+}, V^{4+} and V^{3+}, species, the overlapped V 2*p* peaks were deconvoluted into several peaks by searching for the optimal combination of Gaussian bands with the correlation coefficients (r^2) above 0.99 (PeakFit, Version 4.0.6, AISN Software Inc.). The deconvoluted peaks are signed as specific phases of vanadia (V^{5+}, V^{4+}, V^{3+}) in each spectrum (Fig. 8). The relative percentages of V^{n+}/M', $(V^{3+} + V^{4+})/V^{n+}$, V^{3+}/V^{n+}, and V^{4+}/V^{5+} species were calculated by the area ratio of the corresponding characteristic peaks. The results are listed in Table 3.

Fig. 8 shows the deconvoluted V 2*p* photoelectron peaks of as-synthesized vanadia-based FSP catalysts. The V 2*p* peaks demonstrate broadening of the line with alumina, titania, and ceria doping compared to the zirconia doping. This broadening of XPS peaks can be attributed to various factors including the presence of more than one type of V^{5+} or V^{4+} species with different chemical characteristics, which cannot be distinguished by the XRD, and normal XPS spectra, and the electron transfer between the active component and the support [54]. As can be envisaged from Fig. 8 and Table 3, as-synthesized V/ZrO_2 sample primarily consists of V^{5+} species due to the formation of ZrV_2O_7 solid solution. It has established in our previous studies that the addition of vanadia content to the zirconia led to the formation of ZrV_2O_7 solid solution as a result of zirconia migration into the V_2O_5 crystallites. The introduction of Zr (seven fold coordination) into V_2O_5 may lead to the reduction of elemental number in crystal grain and deviation of adjacent oxygen atoms. Hence, the present XPS studies are in highly agreement with our previous studies, and the SCR activity results of Zr-modified catalysts. There is also a small presence of V^{4+}, V^{3+} species in the V/ZrO_2 catalyst. In all the cases except Zr-doped, as-prepared catalyst surfaces were V^{4+} enriched, as depicted by the consistently higher value of V^{4+}/V^{5+}, V^{4+}/V^{n+} surface. More specifically, in Al_2O_3 doped V-based ($V/TiO_2–AlO_3$, V/AlO_3, $V/CeO_2–AlO_3$) catalysts, V^{4+} species are most enriched over the TiO_2, Al_2O_3 surfaces, V^{3+} species are most enriched over the Al_2O_3 surface relative to that of other catalysts.

Table 3 shows the atom percentage of catalysts determined by XPS. The relative atomic percentage value of V^{4+}/V^{5+}, V^{4+}/V^{n+}, $(V^{3+} + V^{4+})/V^{n+}$characterized by XPS was significantly high for the $V/TiO_2–Al_2O_3$, V/Al_2O_3, $V/CeO_2–Al_2O_3$) catalysts (Table 3 and Fig. 8). The formation of surface V_2O_3 species is improved a lot by the addition of Al_2O_3 (V^{3+}/V^{n+} = 0.36, 0.38, and 0.41 for $V/TiO_2–Al_2O_3$, V/Al_2O_3, $V/CeO_2–Al_2O_3$, respectively), whereas, the addition of TiO_2 led to the formation of surface VO_2 species (V^{4+}/V^{5+} = 0.88, 1.57 for V/TiO_2, $V/TiO_2–AlO_3$, respectively). Among all the catalysts, high surface $(V^{3+} + V^{4+})/V^{n+}$, and V^{4+}/V^{n+} concentrations were observed for the $V/TiO_2–Al_2O_3$, V/Al_2O_3, $V/CeO_2–Al_2O_3$, respectively. It is remarkable to note that the SCR performance of all the as-prepared catalysts is indeed correlated with the surface $(V^{3+} + V^{4+})/V^{n+}$, and V^{4+}/V^{5+} concentrations (Fig. 9). Our TPR results also suggest that the vanadium might have stabilized as the V^{+4}, V^{3+} oxidation states on the Al_2O_3 support up to monolayer coverage, probably due to removal of a bridge oxygen from a V—O—V linkage in a dimeric surface vanadia species, as has

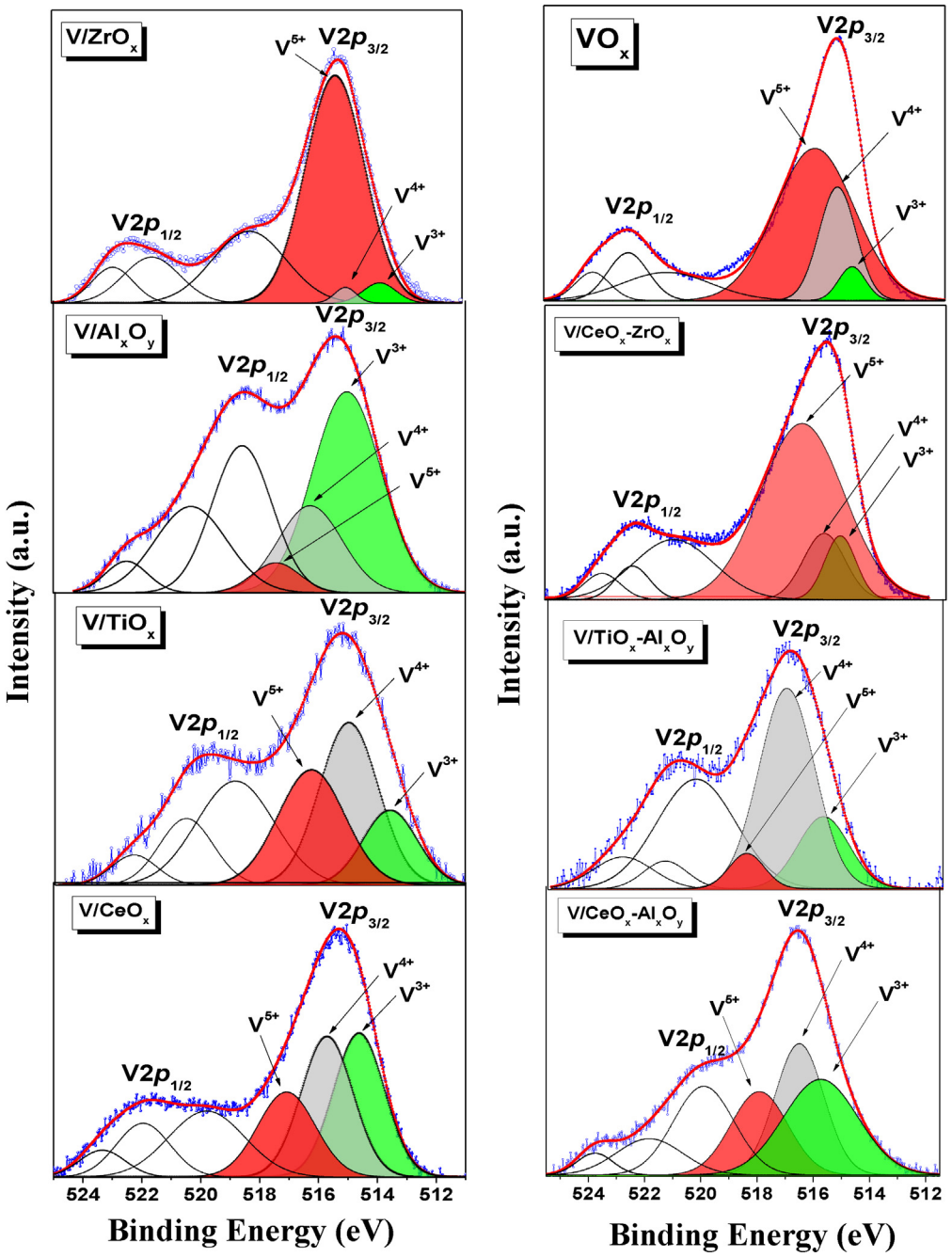

Fig. 8. Deconvoluted V 2*p* (XPS) spectra of (a) V/CeO_2, (a) V/TiO_2, (c) V/Al_2O_3, (d) V/ZrO_2 (e) $V/CeO_2–Al_2O_3$, (f) $V/TiO_2–Al_2O_3$ (g) $V/CeO_2–ZrO_2$, and (h) pure VO_x catalysts.

Table 3
Binding energy, surface atomic ratio of V^{4+}/V^{n+}, V^{3+}/V^{n+}, V^{4+}/V^{5+}, and $(V^{3+}+V^{4+})/V^{n+}$ for all the as-prepared catalysts determined from deconvoluted XPS spectra.

Catalyst	Binding energy (eV)							(V^{4+}/V^{n+})[b]	V^{3+}/V^{n+}[b]	V^{4+}/V^{5+}[b]	$(V^{3+}+V^{4+})/V^{n+}$[b]>
		V2*p*		M′[a]							
	O 1s	V 2$p_{3/2}$	V 2$p_{1/2}$								
V–Al	530.0	517.4 ± 0.1	524.6 ± 0.1	Al 2*p* 75.21	–	–	–	0.35	0.38	1.34	0.73
V–Ce	530.0	517.4 ± 0.1	524.6 ± 0.1	Ce 3$d_{5/2}$ 886.33	Ce 3$d_{3/2}$ 904.46	–	–	0.32	0.31	0.89	0.64
V–Ti	530.0	517.4 ± 0.1	524.6 ± 0.1	Ti 2$p_{3/2}$ 459.46	Ti 2$p_{1/2}$ 464.80	–	–	0.32	0.30	0.87	0.62
V–Zr	530.0	517.4 ± 0.1	524.6 ± 0.1	Zr 3$d_{5/2}$ 181.96	Zr 3$d_{3/2}$ 184.31	–	–	0.18	0.29	0.35	0.47
V–Ce–Zr	530.0	517.4 ± 0.1	524.6 ± 0.1	Ce 3$d_{5/2}$ 885.33	Ce 3$d_{3/2}$ 904.95	Zr 3$d_{5/2}$ 182.09	Zr 3$d_{3/2}$ 184.36	0.26	0.19	0.49	0.46
V–Ti–Al	530.0	517.4 ± 0.1	524.6 ± 0.1	Al 2*p* 74.66	–	Ti 2$p_{3/2}$ 459.44	Ti 2$p_{1/2}$ 464.78	0.39	0.35	1.57	0.75
V–Ce–Al	530.0	517.4 ± 0.1	524.6 ± 0.1	Ce 3$d_{5/2}$ 887.13	Ce 3$d_{3/2}$ 905.39	Al 2*p* 75.27	–	0.27	0.41	0.85	0.68

[a] Binding energy of various support metals.
[b] Relative amounts are according to the metal atomic ratio.

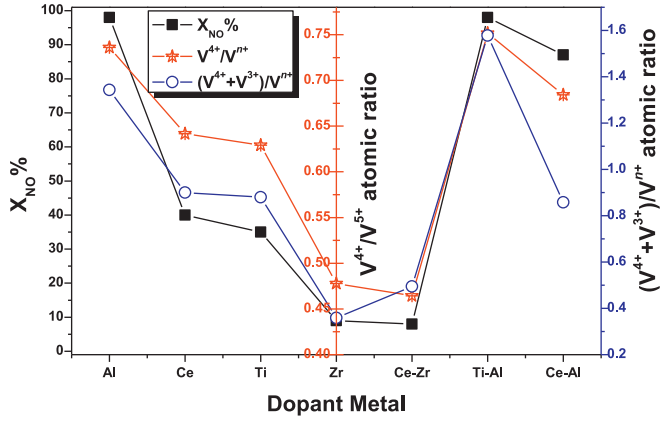

Fig. 9. Surface atomic concentration of V^{4+}/V^{5+} and the surface atomic ratio of $(V^{4+}+V^{3+})/V^{n+}$ with respect to the V/M′ atomic ratio = 0.17 in the catalyst acquired from the XPS analysis: direct correlation of SCR activity of the particular catalyst with the surface atomic concentrations.

been previously reported by the Nag et al. [54] and Haber et al. [50] over the Al_2O_3. Our TPR, XRD results and catalytic activity results are also in highly agreement with these XPS studies.

3.5. Low-temperature catalytic reduction of NO with NH_3 over vanadia flame-made catalysts

In order to compare the influence of dopant (Ce, Al, Zr, Ti, Ce–Zr, Ti–Al, and Ce–Al) cations and activities of flame-made V/M′ nanoparticles were also evaluated for the NH_3-SCR at low-temperatures. However, as proposed from our earlier studies [3], the optimum atomic ratio of the V/M′ = 0.17 was used in the present investigation to reach surface monolayer coverage. The promotion effect of zirconium is very low in the temperature range 140–220 °C as well as catalyst deactivated at above 220 °C (Fig. 10). The V/Ce–Zr catalyst also showed an inhibition in NO conversions and drastic decline in catalytic activity at above 220 °C. This is due to the formation of low crystalline ZrV_2O_7 solid solution in zirconia-based vanadia nanoparticles, which is not visible in the XRD spectra. The observations described in the literature provide interesting information about the reactivity of vanadia toward the ZrXO4 compound

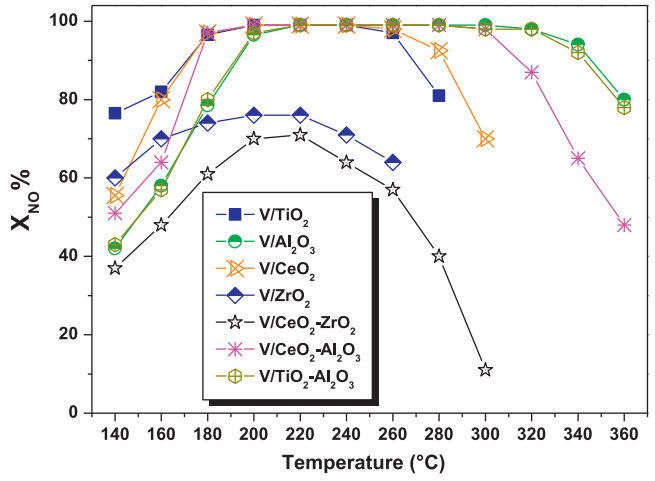

Fig. 10. Influence of various supports on NO conversion in the SCR reaction of V/M′ (M′ = Ce, Ti, Al, Zr, Ce–Zr, Ti–Al, and Ce–Al) catalysts (with consistent V content V/M′ = 0.17) with respect to the temperature; GHSV = 24,000 h^{-1}; feed: NO = 400 ppm, NH_3 = 400 ppm, O_2 = 2 vol.%, He carrier gas, X_{NO}% = conversion of NO at 6 h on stream.

(X = metal). As envisaged earlier [55,56], the vanadia reacts preferably with the ZrO_2 portion of $ZrXO_4$ compound to form the ZrV_2O_7 as shown in the subsequent Eqs. (5) and (6):

$$ZrXO_4 + V_2O_5 \rightarrow ZrV_2O_7 + XO_2 \quad (5)$$

$$ZrO_2 + V_2O_5 \rightarrow ZrV_2O_7 \quad (6)$$

The introduction of Zr (seven fold coordination) into V_2O_5 leads to the reduction of elemental number in crystal grain and deviation of adjacent oxygen atoms and the formation of zirconium pyrovanadate (ZrV_2O_7). It is a fact that the ionic radius of V^{5+} (0.065 nm) are smaller than that of Zr^{4+}(0.079 nm), so it is easier for V^{5+} to incorporate into ZrO_2 lattice to generate zirconium pyrovanadate (ZrV_2O_7) solid solution. The change in lattice parameter, crystal anisotropy and negative thermal expansion of ZrV_2O_7 can block the release of labile oxygen, this seems to be the reason for the decrease in catalytic activity in Zr-modified vanadia flame-made catalysts. These results are in highly consistent with our XPS results where the V/Ce–Zr, V/Zr showed dominant atomic concentrations of V^{5+}/V^{n+} = 0.56, 0.52, respectively. Fig. 10 shows the NO conversions over the Al-modified V/Al, V/Ti–Al, and V/Ce–Al catalysts in the temperature range of 140–360 °C with the function of V/M′ = 0.17 atomic ratios. All the Al-modified vanadia nanoparticle catalysts showed preeminent NO conversions in the temperature range 180–340 °C. The addition of Al to the flame-made vanadia catalysts promoted the SCR activity and broadens the temperature window. These catalysts are more prominent, compared with other titania-, zirconia-, ceria-doped vanadium catalysts. The SCR activity of all the as-prepared vanadia catalysts and the promoting effect of doped metals decreased in the following sequence: V–Ti–Al=V–Al ⋙ V–Ce–Al ≫ V–Ce > V–Ti ⋙ V–Zr > V–Ce–Zr.

Conversely, it has been shown in the literature that the valence state of vanadium in the catalysts could indeed affects the catalytic performance. Reduction in +5 oxidation state of vanadium species is responsible for the enhancement in both NO conversion and N_2 selectivity [6–9]. Catalysts having +4, +3 oxidation states of vanadium species show apparent surface Brönsted acid sites and Lewis acid sites, while those catalysts having V^{+5} only possess Lewis acid sites. This lends support to suggested mechanisms where Brönsted acid sites play a crucial role. As we discussed earlier in the introduction part, the key and rate-determining step in the SCR reaction mechanism is assumed to be the activated adsorption of ammonia on the V^{5+}—OH Brönsted acid site, which reduces a nearby V^{5+}=O redox site to V^{n+} (n = 4 or 3). This activated intermediate V^{n+}—OH, is very reactive toward gaseous NO, leads to the products N_2 and H_2O [8–13]. As expected from our XPS analysis, the NO conversions and thermal stability of the vanadia as-prepared catalyst improved greatly by the addition of Al, and Ti–Al mixed oxide. From Fig. 10, it can be suggested that among all the prepared vanadia flame-made catalysts, Al-modified catalysts (V/Al, V/Ti–Al, V/Ce–Al) demonstrated a superior SCR activity, N_2 selectivity and highly improved temperature window.

The SCR activity of the pure titania-doped, ceria-doped vanadia nanoparticles dropped to the lower NO conversions at higher temperatures above 240 °C, it could be possibly due to sintering of the catalyst. However, SCR activity and temperature window of the V/CeO_2 catalyst improved by the addition of aluminum oxide, due to the high dispersion of vanadium nanoparticles over the Al_2O_3–CeO_2 support. It has been established in the literature [18,57,58] that highly dispersed vanadia on the support accelerates the phase transformation by lowering the activation temperatures. Our catalytic evaluation results are in highly consistent with our XPS, XRD, and active particle diameter measurements, where the Al-modified vanadia flame-made catalysts show $(V^{3+}+V^{4+})/V^{n+}$, and V^{4+}/V^{5+} concentrations (Table 3 and Fig. 9).

4. Conclusions

The addition of Al to the flame-made vanadia catalysts promoted the SCR activity and broadens the temperature window. These catalysts are more prominent, compared with other titania-, zirconia-, ceria-doped vanadium catalysts. The SCR activity of all the as-prepared vanadia catalysts and the promoting effect of doped metals decreased in the following sequence: V–Ti–Al=V–Al $\ggg$ V–Ce–Al $\gg$ V–Ce > V–Ti $\ggg$ V–Zr > V–Ce–Zr. In all the cases except Zr-doped, as-prepared catalyst surfaces were V^{4+} enriched, as depicted by the consistently higher value of V^{4+}/V^{5+}, V^{4+}/V^{n+} surface. More specifically, in Al_2O_3 doped V-based (V/TiO_2–AlO_3, V/AlO_3, V/CeO_2–AlO_3) catalysts, V^{4+} species are most enriched over the TiO_2, Al_2O_3 surfaces, V^{3+} species are most enriched over the Al_2O_3 surface relative to that of other catalysts. It is remarkable to note that the SCR performance of all the as-prepared catalysts is indeed correlated with the surface $(V^{3+} + V^{4+})/V^{n+}$, and V^{4+}/V^{5+} concentrations. Also, TPR is a suitable tool to characterize the surface structures and dispersion of supported vanadia flame spray pyrolysis nanoparticles. The use of V/Al, V/T–Al, V/Ce–Al ($V/M' = 0.17$ atomic ratio) catalysts for the low-temperature SCR of NO with NH_3 is quite promising. The XRD, BET studies revealed that the V loading into Al_2O_3, Al_2O_3–TiO_2, and CeO_2–Al_2O_3 supports favors the formation of highly dispersed surface vanadia nanoparticles (5.8–9.4 nm), whereas, the V doping into ZrO_2, CeO_2–ZrO_2 and CeO_2 led to the primary particle size (19–45.5 nm, formation of bulk particles) growth and thus inhibition in the catalytic activity. A direct relationship between active vanadia particle size and the SCR activity of vanadia nanoparticles has been indicated.

Acknowledgements

The authors wish to acknowledge financial support from the National Science Foundation (Grant No. NSF-0828226), and Prof. M. Rodica and Prof. J. Jacek (University of Louisville) for assistance with the XPS measurements.

References

[1] B. Schimmoeller, S.E. Pratsinis, A. Baiker, ChemCatChem 3 (2011) 1234–1256.
[2] L. Lietti, J. Svachula, P. Forzatti, G. Busca, G. Ramis, F. Bregani, Catalysis Today 17 (1993) 131.
[3] T. Boningari, R. Koirala, P.G. Smirniotis, Applied Catalysis B: Environmental 127 (2012) 255–264.
[4] N.-Y. Topsøe, J.A. Dumesic, H. Topsøe, Journal of Catalysis 151 (1995) 241.
[5] N.-Y. Topsøe, Science 265 (1994) 1217.
[6] D.A. Peña, Doctoral Thesis, University of Cincinnati, 2003.
[7] P. Malet, A. Munoz-Paez, C. Martin, V. Rives, Journal of Catalysis 143 (1992) 47–57.
[8] N.V. Economidis, Master's Thesis, University of Cincinnati, 1998.
[9] N.V. Economidis, D.A. Peña, P.G. Smirniotis, Applied Catalysis B: Environmental 23 (1999) 123–134.
[10] N.-Y. Topsøe, H. Topsøe, J.A. Dumesic, Journal of Catalysis 151 (1995) 226.
[11] I.E. Wachs, G. Deo, B.M. Weckhuysen, A. Andreini, M.A. Vuurman, M. de Boer, M.D. Amiridis, Journal of Catalysis 161 (1996) 211.
[12] J.A. Dumesic, N. Topsøe, H. Topsøe, Y. Chen, T. Slabiak, Journal of Catalysis 163 (1996) 409.
[13] M. Anstrom, J.A. Dumesic, N.-Y. Topsøe, Catalysis Letters 78 (2002) 281.
[14] G. Ertl, H. Knozinger, J. Weikamp, Handbook of Heterogeneous Catalysis, Wiley-VCH, Weinheim, Germany, 1997.
[15] I.T. Horvath, Encyclopedia of Catalysis, Wiley, New York, 2003.
[16] B.M. Weckhuysen, D.E. Keller, Catalysis Today 78 (2003) 25.
[17] J.L.G. Fierro, Metal Oxides, Taylor & Francis, London, 2006.
[18] G.C. Bond, S.F. Tahir, Applied Catalysis 71 (1991) 1 (and references cited therein).
[19] R. Delaigle, D.P. Debecker, F. Bertinchamps, E.M. Gaigneaux, Topics in Catalysis 52 (2009) 501–516.
[20] S. Krishnamoorthy, J.P. Baker, M. D, Amiridis in Annual Meeting of the American-Institute-of-Chemical-Engineers, Elsevier Science BV, Chicago, Illinois, 199839–46.
[21] I. Giakoumelou, V. Parvulescu, S. Boghosian, Journal of Catalysis 225 (2004) 337.
[22] J.P. Dunn, H.G. Stenger Jr., I.E. Wachs, Journal of Catalysis 181 (1999) 233.
[23] .P. Dunn, H.G. Stenger Jr., I.E. Wachs, Catalysis Today 51 (1999) 301.
[24] H. Bosh, F. Janssen, Catalysis Today 2 (1988) 39 (and references cited therein).
[25] Environmental catalysis, in: J.N. Armor (Ed.), in: ACS Symposium Series, 552, Am. Chem. Society, Washington, DC, 1994.
[26] M. Amiridis, R. Duevel, I.E. Wachs, Applied Catalysis B: Environmental 23 (1999) 111.
[27] L. Madler, H.K. Kammler, R. Mueller, S.E. Pratsinis, Journal of Aerosol Science 33 (2002) 369–389.
[28] S. Su, A. Bell, Journal of Physical Chemistry B 102 (1998) 7000–7007.
[29] D. Gazzoli, S. Rossi, G. Ferraris, G. Mattei, R. Spinicci, M. Valigi, Journal of Molecular Catalysis A: Chemical 310 (2009) 17–23.
[30] E.P. Reddy, R.S. Varma, Journal of Catalysis 221 (2004) 93–101.
[31] J. Rack, S. Guk, Y. Il, S. Hayashi, Journal of Catalysis 159 (1996) 170–177.
[32] C. Hu, Z. Zhang, H. Liu, P. Gao, Z.L. Wang, Nanotechnology 17 (2006) 5983–5987.
[33] E.P. Reddy, E. Neeraja, M. Sergey, P. Boolchand, P.G. Smirniotis, Applied Catalysis B: Environmental 76 (2007) 123–134.
[34] Joint Committee on Powder Diffraction Standards (JCPDS), card no: 38-1479; α-Al_2O_3: JCPDS 46-1212; γ-Al_2O_3: JCPDS 29-1486.
[35] T.L. Thomson, J.T. Yates, Chemical Reviews 106 (2006) 4428.
[36] G. Colón, J.M. Sánchez-España, M.C. Hidalgo, J.A. Navío, Journal of Photochemistry and Photobiology A: Chemistry 179 (2006) 20.
[37] K.J.A. Raj, B. Vishwanathan, Indian Journal of Chemistry 48 (2009) 1378–1382.
[38] H. Bosch, B.J. Kip, J.G. van Ommen, P.J. Gellings, Journal of the Chemical Society, Faraday Transactions 1 (80) (1984) 2479.
[39] B. Schimmoeller, H. Schulz, A. Ritter, A. Reitzmann, B.K. Czarnetzki, A. Baiker, S.E. Pratsinis, Journal of Catalysis 256 (2008) 74–83.
[40] S.A. Song, K.Y. Jung, S.B. Park, Langmuir 25 (2009) 3402–3406.
[41] R. Mueller, L. Mädler, S.E. Pratsinis, Chemical Engineering Science 58 (2003) 1969–1976.
[42] H.C. Chang, S.J. Kim, H.D. Jang, J.W. Choi, Colloids and Surfaces A: Physicochemical and Engineering Aspects 313 (2008) 282–287.
[43] M.M. Koranne, J.G. Goodwin, G. Marcelin, Journal of Catalysis 148 (1994) 369–377.
[44] Q. Fu, A. Weber, M.F. Stephanopoulos, Catalysis Letters 77 (2001) 1–3.
[45] H.W. Jen, G.W. Graham, W. Chun, R.W. McCabe, J.P. Cuif, S.E. Deutsch, O. Touret, Catalysis Today 50 (1999) 309.
[46] W. Liu, M.F. Stephanopoulos, Journal of Catalysis 153 (1995) 304.
[47] L. Kundakovic, M.F. Stephanopoulos, Journal of Catalysis 179 (1998) 203.
[48] Y. Li, Q. Fu, M.F. Stephanopoulos, Applied Catalysis B 27 (2000) 179.
[49] M. Inomata, A. Miyamoto, Y. Murakami, The Journal of Physical Chemistry 85 (1981) 2372.
[50] J. Haber, A. Kozlowska, R. Kozlowski, Journal of Catalysis 102 (1986) 52.
[51] F.J.J.G. Janssen, F.M.G. van den Kerkhof, H. Bosch, J.R.H. Ross, Journal of Physical Chemistry 91 (1987) 5921.
[52] M. Demeter, M. Neumann, W. Reichelt, Surface Science 454–456 (2000) 41–44.
[53] G. Silversmit, D. Depla, H. Poelman, G.B. Marin, R.D. Gryse, Journal of Electron Spectroscopy and Related Phenomena 135 (2004) 167–175.
[54] N.K. Nag, F.E. Massoth, Journal of Catalysis 124 (1990) 127.
[55] B.M. Reddy, B. Manohar, S. Mehdi, Journal of Solid State Chemistry 97 (1992) 233.
[56] B.M. Reddy, B. Chowdhury, I. Ganesh, E.P. Reddy, T.C. Rojas, A. Fernández, Journal of Physical Chemistry B 102 (1998) 10176–10182.
[57] A. Vejux, P.J. Courtine, Solid State Chemistry 23 (1978) 93.
[58] R. Kozlowski, R.F. Pettifer, J.M. Thomas, Journal of Physical Chemistry 87 (1983) 5176.